Tissue imaging with coherent anti-Stokes Raman scattering microscopy

"As spontaneous Raman spectroscopy has blossomed and grown during one half-century, it may be predicted with some confidence that coherent nonlinear Raman spectroscopy will yield many new results in the next half-century."
Nicolas Bloembergen, 1978

1. From spontaneous to coherent Raman spectroscopy

Sir Chandrasekhara Venkata Raman was justifiably excited when he noticed that when a monochromatic light beam is passed through a simple transparent liquid, different colors can be detected in the scattered light. Raman called this frequency-shifted scattered light 'a new type of secondary radiation', because he realized that the phenomenon he discovered was caused by a molecular property different from the property of fluorescence emission.[1] Since Raman's early work in 1928, it has been well established that molecular vibrations are responsible for the observed frequency-shifts in the scattered light. The discovery of the Raman effect was only the beginning of a broad and growing branch of molecular spectroscopy, with new applications that continue to emerge to this day, some of which are presented in this book.

Raman's excitement was mirrored almost 35 years later when researchers inserted a cell with transparent liquid, nitrobenzene, in the cavity of a pulsed ruby laser. To their surprise, they observed that the laser output consisted of frequency-shifted components in addition to the radiation at the lasing frequency.[2, 3] Similar to Raman scattered light, this new radiation was seen at frequency shifts that correspond to the frequencies of molecular vibrations. Unlike the incoherently scattered light seen by Raman, however, the frequency-shifted emission from the ruby laser exhibited a well-defined propagation direction and coherence. In analogy with the principle of stimulated fluorescence on which the ruby laser was based, the name stimulated Raman scattering was coined to describe this newly discovered phenomenon. The field of coherent Raman scattering was born.

The frequency-shifted components on the ruby laser output appeared at lower energies, and are thus Stokes-shifted. On closer inspection, however, coherent components at higher energies were also found. Minck *et al* theorized that these anti-Stokes contributions resulted from a cascaded process in the Raman active medium.[4] In this process, the ruby laser wavelength at frequency ω_0 was first shifted to lower frequencies $\omega_0 - \omega_r$ through the stimulated Raman process, where ω_r are the frequencies corresponding to the Raman active vibrations of the molecule. Once a $\omega_0 - \omega_r$ beam has built up in the cavity, it is able to combine with the fundamental frequency and generate new frequency components at $\omega_0 + \omega_r$, i.e. coherent anti-Stokes radiation.[4]

Nonetheless, in Minck *et al*'s experiment several stimulated Raman processes took place in the laser cavity simultaneously, which made it difficult to isolate the generation of the anti-Stokes components from the generation of the red-shifted Stokes contributions. Two years later, Maker and Terhune from the Ford Motor Company were able to generate

coherent anti-Stokes radiation outside of a laser cavity.[5] In their experiment, the required red-shifted $\omega_0 - \omega_r$ component was generated from the fundamental laser beam through a stimulated Raman process in a cell of a Raman active medium. Both beams were then collinearly focused into the sample. Maker and Terhune observed a clear signal at $\omega_0 + \omega_r$. Moreover, they showed that the strength of the signal depended on the presence of a vibrational resonance in the sample at ω_r, which demonstrated the potential of anti-Stokes generation as a molecular spectroscopic tool.

The efficiency of the coherent anti-Stokes generation process depends on the ability of the sample material to respond to three optical frequencies by producing an oscillatory electronic motion at a fourth frequency, which is a combination frequency of the three incoming optical fields. This material property is called the third order susceptibility and is written as $\chi^{(3)}$.[6, 7] The third order susceptibility is composed of parts that depend on the presence of a vibrational mode and parts that are purely electronic in nature, which are known as the resonant and nonresonant contributions, respectively. For spectroscopic measurements, the resonant part $\chi_r^{(3)}$ is of interest, which was the subject of extensive study in early experiments on the nonlinear properties of solids and liquids.[8-10] In 1974, Begley *et al* summarized the most important advantages of vibrational spectroscopy based on nonlinear anti-Stokes generation.[11] First, the coherent anti-Stokes mechanism offers signals that are over five orders of magnitude stronger relative to spontaneous Raman scattering. Second, this nonlinear technique avoids interference with a one-photon excited fluorescence background that often plagues conventional Raman measurements. By baptizing the technique with the name coherent anti-Stokes Raman spectroscopy (CARS), Begley advertised the method as an attractive tool for rapid vibrational spectroscopy.

The much stronger signals compared to spontaneous Raman scattering has made CARS the method of choice for the rapid identification of chemicals present in flames and combustion processes.[12, 13] An added advantage of CARS is that the signal strength is also temperature dependent, which enables an accurate temperature analysis of hot gases and flames.[14, 15] Thermometry and chemical analysis of hot gases continues to be one of the major applications of the CARS technique.

The technique received a next boost when the advent of ultrafast picosecond lasers opened up the possibility of directly time-resolving the vibrational relaxation of selective molecular modes.[16] The broad bandwidth pulses that became available when femtosecond lasers entered the laboratories of spectroscopists enabled furthermore the coherent excitation of multiple Raman modes.[17-19] In femtosecond CARS, the time-resolved signal typically displays oscillatory features, which is a direct manifestation of mutual destructive and constructive interferences, often called quantum beats, between the different modes. Using Fourier transform methods, the time-resolved CARS trace can be related to the Raman spectrum. Femtosecond CARS on nonabsorbing substances can thus be seen as a form of Fourier transform Raman spectroscopy.

Although CARS is a third order nonlinear process, the technique is unable to resolve information beyond what is contained in the Raman spectrum, such as the mutual coupling between vibrational modes. To observe such couplings, higher order coherent Raman experiments are required.[20] When applied to systems with electronic resonances,

however, femtosecond CARS may reveal information on time-dependent vibronic relaxation, which cannot be probed with spontaneous Raman scattering techniques.[21] These advantages have kept the popularity of time-resolved CARS spectroscopy as a probing tool for the ultrafast molecular dynamics in the condensed phase at a high level.

2. The birth of CARS microscopy

2.1. First generation CARS microscopes

In microscopy, signals are collected from many spatially resolved locations in the sample, yielding images that typically consist of several thousands to millions of pixels. Microscopic imaging is thus based on the collection of many individual measurements, either sequentially or in parallel. With such a large number of measurements, optical microscopy relies on a contrast mechanism that is associated with a high photon flux. To build a microscope based on vibrational contrast, the CARS mechanism is a natural candidate, as the signal yields are much higher than what the spontaneous Raman scattering process can offer. The first Raman microscope was conceived in 1975[22], but long image acquisition times had hampered the application of this approach for imaging of dynamic samples such as live biological specimens. In the early 1980's, Duncan *et al* recognized the potential advantage of CARS microscopy over the existing Raman microscope in terms of imaging speed. In 1982, they constructed the first CARS microscope.[23]

The system built by Duncan *et al* was fuelled by two visible picosecond dye lasers that provided the pump ($\omega_p \equiv \omega_0$) and Stokes ($\omega_S \equiv \omega_0 - \omega_r$) beams for the CARS process (see Figure 1). Before the beams were focused to a 10 μm spot, a scanning mirror applied an adjustable angle to the incident radiation, which enabled lateral motion of the focal spot over a 300 μm range. Unlike the early CARS work of Maker and Terhune, the pump and Stokes beams were not arranged in a collinear geometry in this early nonlinear microscope. Instead, Duncan *et al* chose to adopt a noncollinear arrangement of the beams. Such a geometry had become commonplace for CARS measurements in condensed phase materials, which was motivated by extending the interaction length over which the pump, Stokes and anti-Stokes waves stay in phase during the signal generation process.[24] Indeed, noncollinear excitation geometries extended the range of phase-matching between the waves from less than a hundred microns to up to several centimeters.

Although the anti-Stokes signal was generated from a relatively large diameter focal spot, the spatial resolution of the first CARS microscope was determined by the collection optics rather than the focusing lens. The CARS light was captured by a microscope objective, filtered by a stack of spectral filters and projected onto a camera placed in the image plane, yielding images with sub-micron resolution. The imaging speed of the CARS microscope lived up to the expectations: within only 2s, vibrationally sensitive images of a 200 x 200 mm area at microscopic resolution were shot, clearly claiming superiority over the much slower Raman microscope. However, the spectral

contrast was rather disappointing. Only after use of image subtraction techniques could deuterated lipids in dense liposomes clusters be discriminated from their non-deuterated counterparts.[25, 26] The gain in speed relative to the Raman microscope was compromised by a significant loss in vibrational contrast, casting some serious doubts on the practical benefits of CARS microscopy.
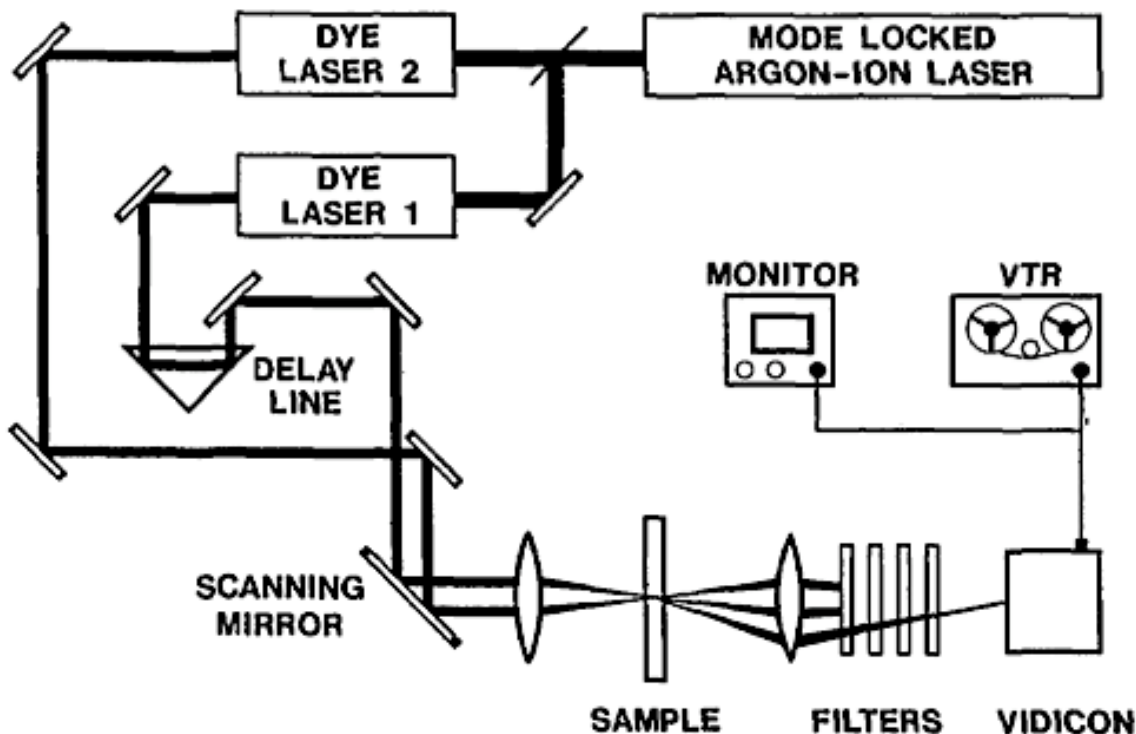

Figure 1: The first CARS microscope built at the Naval Research Laboratory in 1982 by Duncan et al. Note that a noncollinear beam geometry was used and that the high resolution was attained by the high numerical detection lens. Reproduced from Duncan et al., *Optics Letters* **7**, 350-352 (1982) with permission of the Optical Society of America.

2.2. Second generation CARS microscopes

The low contrast in the first CARS microscopes was caused by the presence of a strong nonresonant background. Scholten *et al*, who built the first wide-field CARS microscope[27], proposed several possible background rejection mechanisms, among which resonant enhanced CARS[28] and background cancellation by phase-mismatching.[29] But was not until 1999, 18 years after the inception of CARS microscopy, that the technique was fortuitously resuscitated by Zumbusch *et al* and was saved from becoming a dust collecting curiosity.[30] Key to the success of the second generation of CARS microscopes was the reintroduction of the collinear excitation geometry. Zumbusch *et al* realized that when the incident beams are focused by a high numerical aperture microscope objective, the interaction length between the pump, Stokes and anti-Stokes fields is so short that the waves are unable to run out of phase. Hence, there is no need for a noncollinear phase-matching arrangement of the beams per se.[31] With the collinear arrangement, smaller and cleaner focal volumes are produced, which condenses the location of CARS signal

generation to a sub-micrometer spot in the sample. CARS generation in small, phase-matched volumes has two important advantages: 1) the microscope has an intrinsic three-dimensional resolution because of the confinement of the interaction volume in both the lateral and axial dimensions, similar to the two-photon extcited fluorescence microscope[32], and 2) reduction of the focal volume assigns more importance to small vibrationally resonant structures relative to the nonresonant signal generated from the bulk. This latter notion is the major reason why the nonresonant background in Duncan's imaging system was overwhelming whereas it is manageable in Zumbusch's collinear excitation microscope where the focal volume is almost three orders of magnitude smaller.

Although image acquisition times in the first incarnation of the collinear CARS microscope were too long for practical biological imaging, within two years subsequent improvements of the light source, the scanning mechanism and the detectors brought the imaging rate down to a couple of seconds per image.[33, 34] Despite the fact that the nonresonant background still imposed contrast challenges, for several imaging applications, most notably the imaging of lipids, the vibrational signal turned out to be strong enough to compose high contrast images. The first applications to visualizing intracellular lipid bodies[35, 36] and membranes[37-40] proved decidedly successful, which spurred the continuously growing popularity of CARS microscopy as a useful visualization tool in cellular biology.

Since 1999, the field of CARS microscopy has grown beyond all expectations. Active CARS research is conducted both on the technological front, which seeks to improve the chemical imaging capabilities, and the applications front. Although CARS imaging has found several applications in material science[41-43], the majority of CARS applications are within the realm of biological and biomedical research. In this Chapter, we will provide examples and prospects CARS in these latter areas. For a more extensive overview of the developments in the CARS microscopy field since 1999, the reader is referred to several excellent review papers in the literature.[44-47]

3. CARS basics

In order to better appreciate the imaging properties of the CARS microscope, we will briefly explain the basic physical principles that underlie this technique. Our discussion will be largely qualitative, with an emphasis on the physical picture rather than their mathematical descriptions. The different principles on which the CARS technique is based are not all conveniently explained within a single framework. Some properties are easily explained within a classical mechanical picture, whereas the clarification of other properties requires a quantum mechanical framework. This dual picture is the source of some confusion about some of the aspects of CARS. In the following, we will exclusively adopt a classical picture to explain the generation of waves at the anti-Stokes frequency. A similar discussion with more mathematical representation can be found elsewhere.[48-50]

3.1. Nonlinear electron motions

In the CARS process, light beams are used with optical frequencies ($\sim 10^{13} - 10^{17}$ Hz), corresponding to wavelengths in the visible and near infrared range. Nuclei in molecules are unable to respond to an electric field that oscillates at such high frequencies. The electrons surrounding the nuclei, however, will respond to the electric field by oscillating at the frequency of the incoming electromagnetic field. For relatively weak electric fields, the electrons respond linearly to the driving field. Under these conditions, the spatial extent of the electronic oscillation is small and the motion in the potential well is harmonic. For stronger fields, however, the electrons are pulled farther from their equilibrium positions and the cloud picks up anharmonic motions. As shown in Figure 2, the response of the electrons to the incoming field is no longer linear. CARS is based on these anharmonic motions of the electron cloud.

If the electrons are driven at two strong optical frequencies simultaneously, the anharmonically oscillating cloud will contain oscillatory motion at combination frequencies. Of relevance to the CARS process is the electron cloud's ability to shake at the difference frequency between the pump and the Stokes fields, i.e. at the beat frequency $\omega_p - \omega_S$. In practice, such oscillations occur in any molecular sample when the pump and Stokes beams are applied, irrespective of the presence of nuclear resonances at $\omega_p - \omega_S$. Whenever the electrons shake at the beat frequency, the electronic properties of the material will be slightly altered relative to the situation when the light beams are absent. More specifically, the refractive index of the material is modulated at the difference frequency. A changing refractive index implies that a third light wave of frequency ω_{pr} that travels through the sample will be scattered. The scattered light will naturally be modulated at the difference frequency, which corresponds to scattered light components at the frequencies $\omega_{pr} \pm (\omega_p - \omega_S)$. In the case that the third light wave is of similar frequency as the pump light, we will thus find anti-Stokes radiation at $2\omega_p - \omega_S$.

This type of anti-Stokes scattering is very different from spontaneous Raman scattering in that the scattered light components are all modulated with the same phase, i.e. the anti-Stokes radiation is coherent. This coherence also implies that the waves add up constructively in a specific direction, and destructively interfere in all other directions, producing radiation with a well-defined propagation direction. In the CARS microscope, the direction in which the waves add-up, i.e. the phase-matching direction, is the forward propagation direction that is collinear with the incident beams. For comparison, because of the lack of coherence, the signal resulting from the spontaneous Raman process is scattered isotropically.
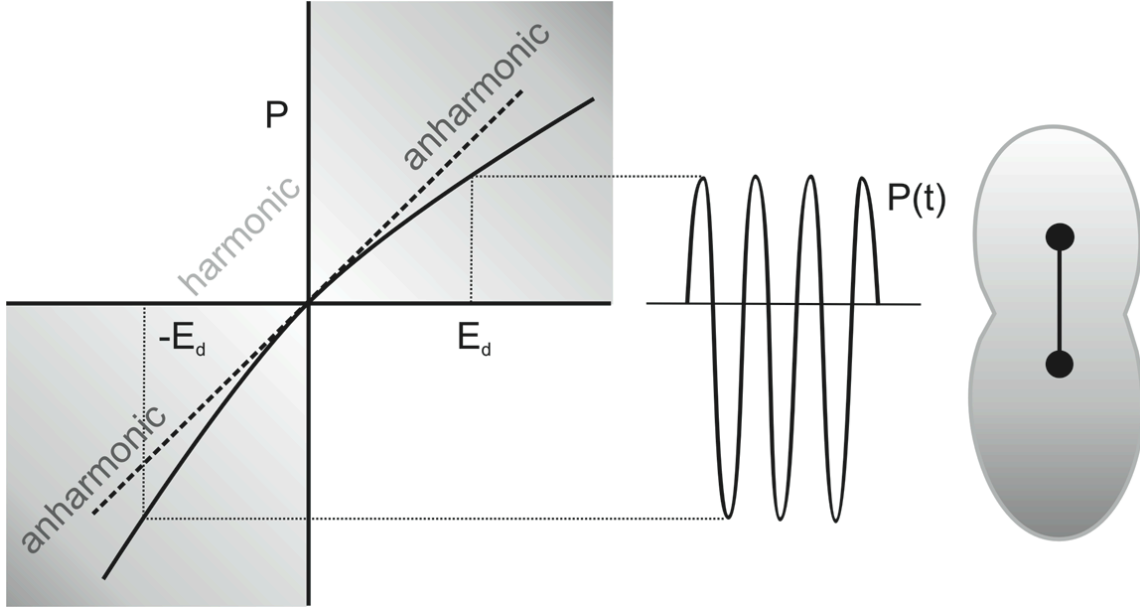
Figure 2: Polarization of the material as a function of the driving field E_d. For stronger fields, the polarization is no longer linearly proportional to the driving field as a consequence of the anharmonicity of the potential in which the electrons reside. Under these conditions, the oscillation amplitude of the polarization is distorted, which is the source of optical nonlinear signals, including CARS.

3.2. Resonant and nonresonant contributions

The process we have discussed so far is responsible for the generation of the nonresonant background in CARS. Clearly, the occurrence of this contribution is purely electronic and bears no dependence on the presence of vibrational modes. Why, then, is the CARS process sensitive to vibrational resonances that are nuclear in nature? This sensitivity stems from the notion that the electrons are bound by a potential that is defined by the location of the nuclei. At some frequencies, namely the nuclear resonance frequencies, this potential becomes more malleable. Consequently, the electron cloud becomes more polarizable at these frequencies. In other words, the presence of nuclear modes perturbs the polarizibility of the molecule's electron density at well-defined frequencies, which can now be shaken into resonance whenever the difference frequency $\omega_p - \omega_S$ matches the nuclear resonance frequency. The oscillation amplitude of the electron cloud will be larger at such frequencies and produce more scattered light at $2\omega_p - \omega_S$.

From this discussion we also see that the CARS process brings about two types of coherent anti-Stokes fields: one field contribution generated from purely electronic motions and one field contribution resulting from electron motions that depend on the presence of nuclear modes. The total CARS signal is the square modulus of the coherent sum of this nonresonant and resonant field component. The coherent mixing of the nonresonant and resonant signals makes it particularly difficult to detect each contribution separately. Many research efforts are devoted to suppressing the nonresonant portion of the CARS signal. Polarization sensitive detection[51, 52], interferometric

mixing[41, 53] and frequency modulation[54] are examples of techniques that reduce the nonresonant background in practical and rapid CARS imaging.

4. CARS by the numbers

4.1. Signal generation in focus with pulsed excitation

Compared to the linear response of materials to optical fields, the third order susceptibility of samples is extremely small. Expressed in electrostatic units, measured values of $\chi^{(3)}$ for condensed phase materials are on the order of $\sim 10^{-14}$ esu.[55] The $\chi^{(3)}$-related changes to the refractive index are of magnitude 10^{-16} cm^2/W, which implies that an optical field with an intensity of 1 W/cm^2 will modify the material's refractive index by only 10^{-16}. Clearly, much stronger optical fields are required to induce a detectable third order nonlinear signal. The high peak powers offered by pulsed excitation provides such electric field strengths.

Keeping the average power constant, increasingly higher peak powers are obtained for increasingly shorter pulses. Consequently, the highest third order signals are obtained for the shortest pulses. The purely electronic (nonresonant) CARS response is indeed maximized for the shortest possible pulse, as it scales as $\sim 1/\tau^2$, where τ is the pulse width.[56] Nonetheless, the ratio of the vibrationally resonant response over the nonresonant signal is decreasing for shorter pulse widths. This is because the not all the frequency components of broader bandwidth pulses combine to drive the vibrational modes at $\omega_p - \omega_S$, whereas all combinations of the spectral components contribute to generate the nonresonant response. A balance between maximum signal generation and an optimized resonant-to-nonresonant signal ratio is found for pulse widths of 2-5 ps.[33] For such temporal widths, the spectral width of the pulses matches the width of the Raman resonances in condensed phase materials, which constitutes the most favorable excitation condition for CARS imaging based on a single Raman band.

When a 5 ps, 800 nm pulse of 0.1 nJ is focused by a water immersion microscope objective with a numerical aperture of 1.2, the peak intensity in focus amounts to 2×10^{11} W/cm^2. Optical fields that correspond to these intensities bring about detectable changes to the refractive index, especially in the phase-matched direction. Under such conditions, the amount of detected CARS signal generated from pure water at the OH-stretching vibration ($\sim$3300 cm^{-1}) can be as high as 500 photons per shot.[34] For sub-micrometer sized objects, such as a lipid bilayer visualized at the CH$_2$-stretching vibration (2845 cm^{-1}), the CARS signals are generally substantially smaller, but still detectable. With similar pulse energies, a bilayer with more than 10^6 CH$_2$ modes in the focal volume can be visualized in the phase-matched forward direction at $\sim$0.1 photons detected per shot. Such photon detection rates are sufficient to produce good quality images recorded with sub-ms pixel dwell times and $\sim$80 MHz pulse repetition rates. For planar lipid membranes detection in the epi-direction is similarly sensitive, with detection sensitivities of less than 10^6 CH$_2$ modes in focus at sub-ms pixel dwell times.[57]

4.2. Photodamaging

Naturally, higher CARS signals are attained by increasing the pulse power. However, photo-damaging concerns put a practical limit on how much power can be applied to the sample. Two types of photo-damage are relevant to this discussion. First, light absorption by components in biological materials, which scales linearly with the average illumination power, produces heating of the sample. Using near-infrared radiation, sample heating is generally negligible for average powers less than 10 mW in most biological materials.[58, 59] Second, nonlinear excitation of compounds in cells and tissues may induce photochemical changes with possible toxic photoproducts, among which the formation of radicals.[58, 60] In CARS studies, nonlinear photo-damage is oftentimes the prime source of damage to the sample.[61] By keeping the pulse energies below 1 nJ, nonlinear photodamage in CARS microscopy can be generally avoided for most samples.[56] In practice, imaging with focal intensities of 10 mW from a ~80 MHz pulse train produces excellent CARS signal levels while photodamaging effects are kept to a minimum.

4.3. CARS chemical selectivity

The CARS imaging microscope has proven to be a very sensitive tool to visualize the distribution of lipids in biological samples. For instance, CARS has been used to follow the growth and trafficking of lipid droplets in a variety of cell types[36, 56] and microorganisms[62], to visualize the agent-induced morphological changes to myelin sheets in the spinal cord[63, 64] and to map out lipid deposits in atherosclerotic lesions.[65] All these studies are facilitated by the high density of CH_2 modes in lipids, which produces a CARS strong signal at its symmetric stretch vibration at 2845 cm^{-1}. The lipid CARS response also benefits from having its major signatures in a relatively quiet region of the vibrational spectrum, which prevents spectral interferences with neighboring bands. Other dense CH_2-containing compounds and a concentrated substance like water can also be relatively easy visualized in the high frequency range (2500 – 3500 cm^{-1}) of the vibrational spectrum. Specificity among lipids and other CH_2-containing compounds can furthermore by obtained through the use of deuterium labels.[25, 57, 66, 67]
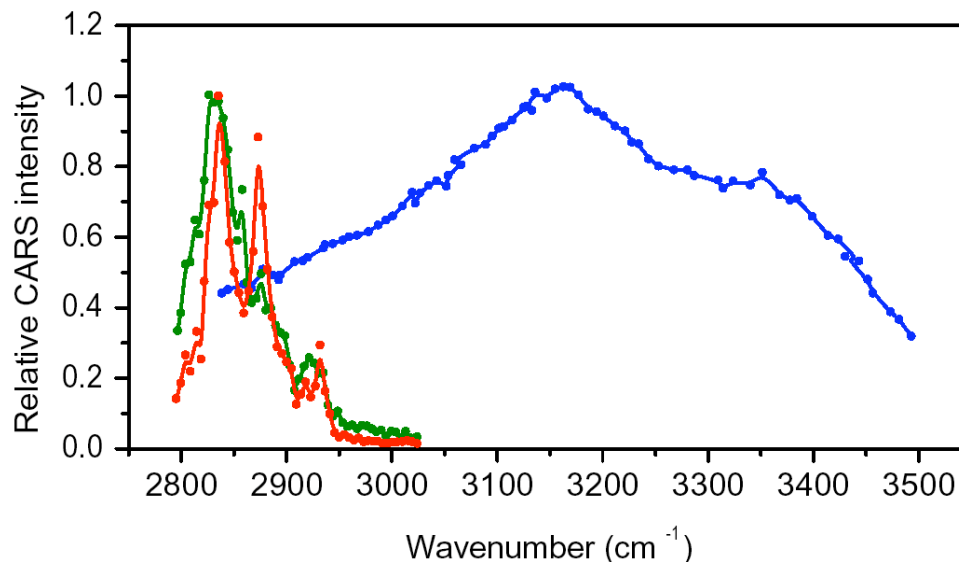
Figure 3: Normalized CARS spectra of common tissue compounds. Cholesterol (green), the lipid tristearin (red) and water (blue) are shown in the region of the vibrational spectrum that includes the CH and OH stretching vibrations.

The situation in the fingerprint region ($\sim$800 – 1800 cm^{-1}) is, however, quite different. Unlike the limited number of molecular modes in the high frequency region, many molecular groups have their frequencies in the fingerprint region. Indeed, a typical Raman spectrum from a biological sample is characterized multiple partially overlapping vibrational bands. Such congested spectra may complicate a clear identification of the molecular compounds, and advanced algorithms such as hierarchical cluster analysis are often required to extract the molecular composition from measured spectra.[68] In CARS, matters are even more complicated. Because each vibrational band carries its own frequency dependent spectral phase, the coherent anti-Stokes Raman spectrum is affected by interferences among the different spectral signatures, in addition to interference with the nonresonant background. As a consequence, the spectral information in CARS spectra from the fingerprint region typically appears featureless and washed out. Much of the interferences can be undone by means of phase retrieval algorithms like the maximum entropy method (MEM), which extracts Raman-like spectra out of congested CARS spectra.[69, 70] With the aid of signal processing tools, CARS spectroscopy in the fingerprint region has several advantages relative to Raman spectroscopy, especially in terms of speed.
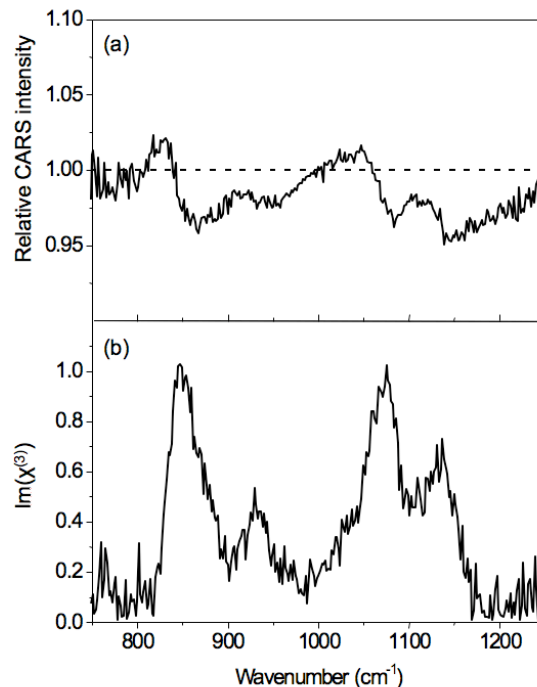
Figure 4: CARS spectrum of an aqueous 50 mM sucrose solution. a) CARS signal in the 800 - 1200 cm^{-1} region relative to the nonresonant background from the buffer solution. Note the washed out spectral contrast due to intereference with the nonresonant electronic signal. b) Retrieved vibrational Raman spectrum [Im($\chi^{(3)}$)] from the CARS data using the maximum entropy phase retrieval method. Clear Raman signatures are discerned in the retrieved spectra. Courtesy of Mischa Bonn, AMOLF, the Netherlands.

For high-speed CARS imaging studies, which rely on the availability of clear signatures to generate image contrast, post-acquisition spectral processing is not always an attractive option. Instead, methods have been developed that aim at direct contrast enhancement of a particular signature through optimized excitation and detection conditions. Heterodyne CARS microscopy, which avoids spectral interferences by detecting the CARS field instead of the intensity, is an example of a technique that can recover spectral signatures that are otherwise unsuitable for imaging.[53, 71] This approach has been used to image proteins through the CH_3 stretching vibrations, which are usually affected by the spectral interferences with the nearby CH_2 symmetric stretch mode.
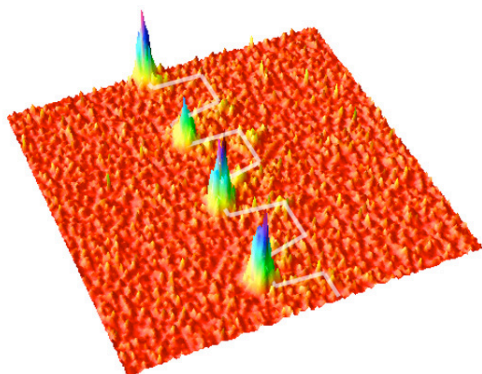
4.4. CARS sensitivity

With regular CARS microscopy, image contrast can be generated based on concentration variations that are less than 10^6 CH_2 oscillators in focus.[57] These numbers translate to about less than 10^5 lipid molecules in the focal volume, which amounts to (sub-)mM concentrations. In many situations, in particular in drug delivery studies, the target molecule is present in the sample at much lower concentrations in a surrounding where variations in nonresonant background levels may be substantial. For these studies, more

sensitive detection methods are required. Frequency modulation (FM-)CARS microscopy is an example of a detection technique that suppresses the nonresonant background and sensitively extracts the vibrationally resonant CARS signal, producing sensitivities of less than 10^6 Raman oscillators in the presence of a considerable nonresonant background.[54] Techniques like FM-CARS have the potential to detect sub-mM concentrations of Raman active agents in actual tissues.

Is CARS a suitable technique for single molecule vibrational spectroscopy? In the case of collective Raman modes, such as can be found in carbon nanotubes, CARS signals can certainly be generated from single structures. In the limit of a single local mode, many of the benefits of CARS disappear. In particular, the coherent addition of emitting Raman oscillators, producing strong signals in phase-matched direction, no longer applies to the single oscillator limit. A theoretical analysis shows that the CARS response is not necessarily stronger than the spontaneous Raman response in this limit, as the emission is essentially incoherent.[72, 73]

These considerations illustrate that CARS microscopy in the single molecule limit requires additional enhancement mechanisms to generate detectable signals. Motivated by the success of surface-enhanced Raman scattering (SERS)[74, 75], researchers have started studies in which the enhanced local fields associated with surface plasmons of metallic substrates are used to boost the CARS response. Because surface plasmon resonances produce an intrinsic electronic anti-Stokes response[76-78], surface enhanced (SE-)CARS may be more challenging than SERS. Nonetheless, past and recent work has indicated that SE-CARS is experimentally feasible and may offer additional ways of probing the vibrational response of molecules, potentially at the single molecule limit.[79-82]
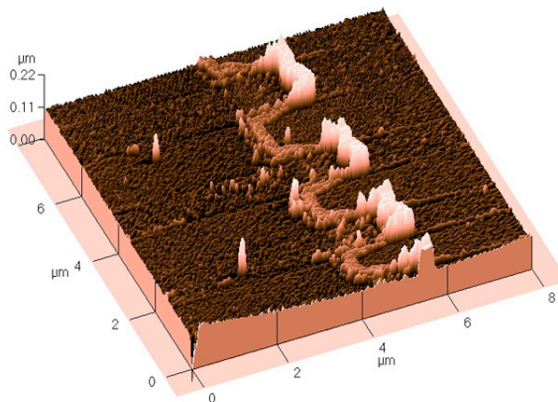

Figure 5: Coherent anti-Stokes image (left) and atomic force microscopy topograph (right) of a gold nanowire sample. This zig-zag nanowire exhibits alternating plateaus with heights of 20 nm and 80 nm, respectively. Note that the higher third order coherent signals from the wire are obtained from the lower plateaus, indicating a stronger electronic plasmon resonance in those regions.

5. CARS and the multimodal microscope

The CARS imaging system is composed of a fast scanning microscope and an ultrafast light source. For generating images quickly, picosecond lasers have been shown to optimize the CARS contrast in the microscope relative to femtosecond excitation.[33] This is particularly true for generating CARS contrast from a relatively narrow (> 10 cm^{-1}) line in the Raman spectrum. Optimum contrast is obtained if the spectral width of the laser pulses complies with the width of the target Raman band. However, for broader vibrational bands - most notably the OH-stretching vibration of water, and, to a lesser extent, the lipid CH_2-stretching spectral range - femtosecond laser beams can be used as well.

The pump and Stokes fields necessary for the CARS process are usually derived from separate light sources. For instance, two synchronized ultrafast Ti:sapphire lasers can be used to deliver the pump and Stokes beams.[33, 83] Alternatively, a synchronously pumped optical parametric oscillator offers a convenient system for producing stable pump and Stokes pulse trains. Besides generating CARS, such ps/fs pulse trains are also conducive for inducing accompanying nonlinear signals in the focal volume of the objective lens. In particular, two-photon excited fluorescence (TPEF) and light resulting from second harmonic generation (SHG) are readily observed in a CARS microscope. Hence, by using additional detectors and appropriate spectral filtering, a multitude of nonlinear signals can be monitored simultaneously. Indeed, in one of the first rapid CARS imaging studies of living cells, the CARS technique was combined with simultaneous two-photon excited fluorescence lifetime microscopy (FLIM).[34] Other examples include multimodal imaging based on CARS, TPEF, SHG and sum frequency generation (SFG) microscopy.[65, 84]

The CARS imaging microscope enables a complete multimodal investigation of tissues based on endogenous contrast. In addition to the chemical selectivity offered by CARS, simultaneously detected SHG signals reveal tissue collagen patterns and TPEF signatures report on endogenous fluorophores such as elastin fibers and nicotinamide adenine dinucleotide (NAD) metabolic agents.[85, 86] The CARS microscope thus constitutes the ultimate nonlinear imaging platform.
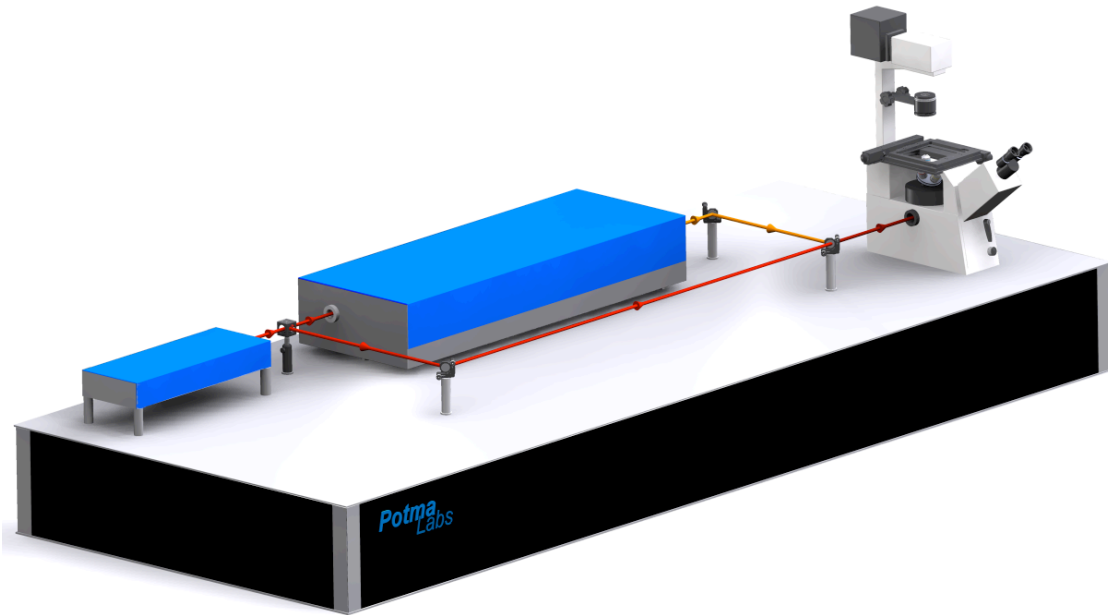
Figure 6: Rendering of a typical multimodal microscope based on a picosecond Nd:Vanadate laser, a synchronously pumped optical parametric oscillator (OPO) and an optical microscope. In such a scheme, the pump beam for the CARS process is delivered by the OPO and the Stokes beam by the Nd:Vanadate laser. The pump and Stokes beam are overlapped in space and time and collinearly directed to the microscope. Scanning of the focal spot is accomplished either by scanning the sample stage or by angle scanning the incident beams.

6. CARS in tissues

The major difference between thin samples (μm-sized) and tissues is the presence of significant light scattering in the latter. Light scattering is a consequence of variations in the linear refractive index in the sample. In tissues, refractive index variations result from large structures such as extracellular fibers and smaller structures such as intracellular organelles in an otherwise aqueous environment. In addition, light absorption is also relevant for thicker tissues. Both light scattering and absorption give rise to signal loss in tissues relative to thin samples. The consequences of these linear optical effects on the CARS signal will be discussed below.

6.1. Focusing in tissues

Optimum CARS signals are obtained when the incoming light is condensed into a tight focal spot. Naturally, light scattering in tissues compromises the formation of a clean

focal spot. The reason for this is two-fold. First, scattering of excitation light in the tissue leads to loss of amplitude in the vicinity of the focal volume.[87-89] Second, the phase of the incident waves will be compromised upon arrival in the focal region. The focal volume, which exists by virtue of constructive interference of light waves in one point in space[90], is very sensitive to the coherence of the incoming light. Loss of phase coherence implies that the waves will be unable to completely interfere to produce a tight focal spot. Hence, in the presence of scattering, the focal volume will be smeared out and contain a lower excitation density. CARS signals are directly affected and generally much lower if tissue scattering is significant.

Using NIR radiation, appreciable CARS signals up to 0.25 mm can generally be produced in most tissue types. Special long working distance objectives can often be used to increase this penetration depth by a factor or two. Beyond 0.5 mm, light scattering severely complicates the formation of a sufficiently tight focal spot for CARS generation. To increase the number of in-phase photons that arrive in the focal volume at greater depths, higher excitation powers can be used. Such an approach has been used to accomplish deep-tissue imaging with two-photon excited fluorescence[91], and is, in principle, also possible for CARS microscopy. Absorption and linear heating of the sample are the limiting factors for applying more power to achieve strong signals at greater depths. The photodamage threshold in pigmented skin, for instance, is found to be 500 W/cm^2.[92] Generally, when keeping sample illumination dosages below 50 mW per beam, imaging well below the damage threshold can be achieved.

Besides lower signals as a consequence of random scattering throughout the tissue, scattering also affects the CARS imaging properties when scattering objects in focus affect the signal generation process. Figure 7 shows an example of how linear refractive index differences in focus compromise the image quality. The image of a paraffin oil droplet in water is severely affected by the refractive index difference between the droplet and its aqueous surrounding ($\Delta n \sim 0.15$). Phase distortions of the incident light along with phase mismatching of the CARS radiation in focus both contribute to the distorted image. When the surrounding is replaced with dimethyl sulfoxide, a fluid with a refractive index closer to that of paraffin oil ($\Delta n = 0.03$), the image appears relatively undistorted. This simple example shows that linear refractive index differences will always affect image appearance in turbid media like tissues. In this regard, a proper understanding of these effects will help the interpretation of the images.
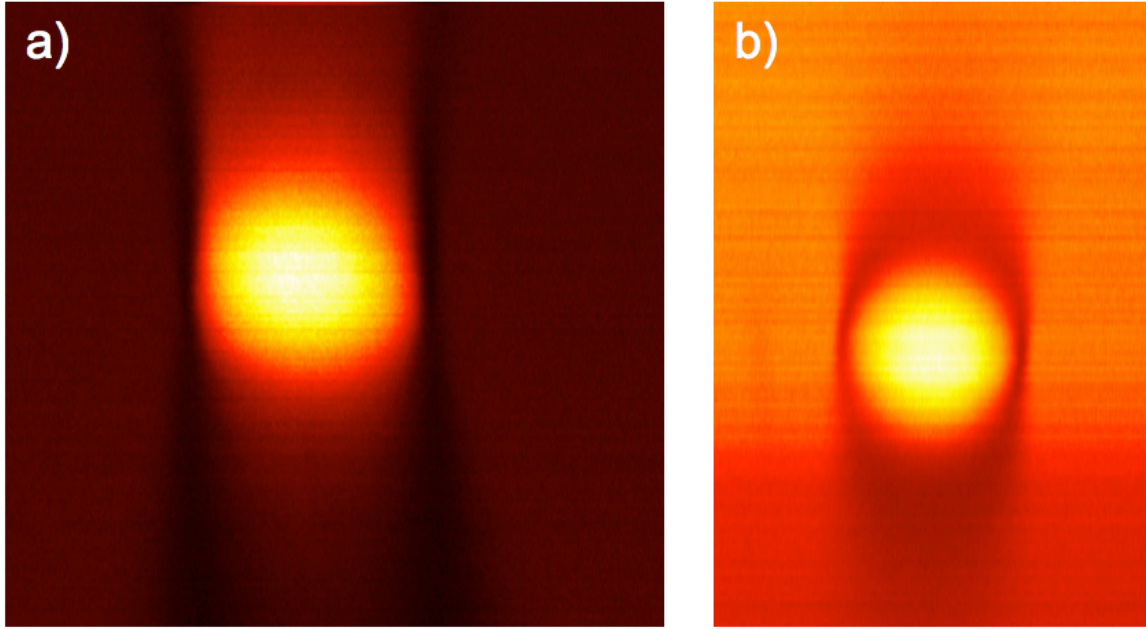
Figure 7: Effect of $\chi^{(1)}$ scattering on coherent $\chi^{(3)}$ signals. a) CARS image of a dodecane droplet in water. Clear vertical shadow edges can be seen in nonresonant signal from the water, which is a direct consequence of linear scattering of light at the dodecane/water interfaces. b) Paraffin droplet in d-DMSO. Because the refractive index differences between paraffin and d-DMSO are minimal, the shadowing effect is much reduced.
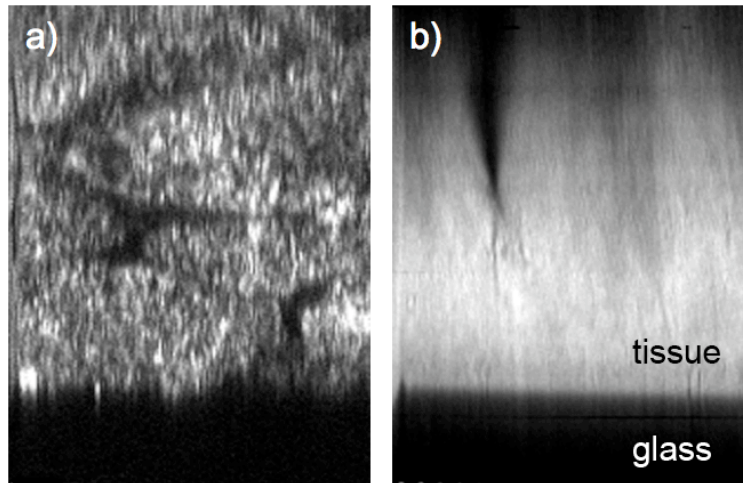

Figure 8: Effect of linear scattering on quality of CARS tissue images. a) Two-photon excited autofluorescence xz-image of chicken breast tissue, excited at 800 nm using a 1.2 NA water immersion lens. Total scan depth is 80 μm. b) Simultaneously detected CARS signal from water. Note that the penetration depth of CARS is less than for two-photon excited fluorescence, and that the coherent third order signal is more sensitive to linear scattering at dense objects. Linear scattering is evident from the apparent shadowing streaks in the image.

6.2. Backscattering in tissues

In addition affecting the incident light and the CARS signal generation process, scattering also acts on the generated CARS light. Although post-generation does not decrease the number of CARS photons produced, it changes the propagation direction of the CARS emission by redistributing it over a large cone angle. Since the unaffected CARS signal is predominantly propagating in the forward direction[93, 94], post-generation scattering will generally lower the amount of photons that can be captured in the forward direction and increase the number of photons that can be intercepted in the backward direction. The latter notion is particularly relevant for CARS imaging in thick tissues when forward detection is limited due to the opacity of the tissue and the signal can only be detected in the backward direction.

In Figure 9 the amount of CARS light that is scattered back from a tissue phantom is plotted as a function of phantom thickness. It is clear that for tissues thicker than a couple of hundred microns, a significant fraction of the forward propagating light is redirected into the epi-direction.[95] Backward scattering of forward propagating CARS light is the major mechanism that enables the collection of appreciable signals in the epi-detection channel. The same principle has also been shown to be important in SHG imaging.[96, 97]
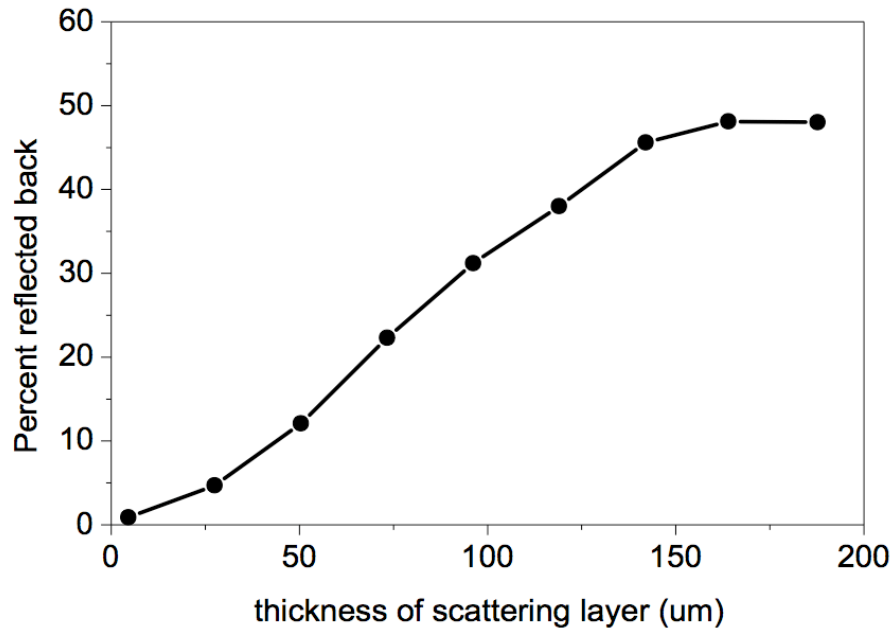

Figure 9: Percent of CARS signal detected in the backward direction as a function of the thickness of the scattering layer. The model scattering layer was a 10% intralipid emulsion. Backscattering of forward propagating coherent radiation is thought to be the major mechanism that contributes to the contrast in CARS tissue images.

6.3. Typical endogenous tissue components

Which important tissue components can be straightforwardly visualized with CARS? Several CH_2-rich structures can be imaged with good contrast in the fast imaging CARS microscope. Figure 10 shows an image taken in the dermis of human skin *ex vivo*. The dermis is rich in structural fibers such as collagen and elastin, which can both be visualized with CARS, as is evident from the Figure. Similar observations have been made in arterial tissue.[84] Alternatively, elastin can be visualized by two-photon excited fluorescence and collagen by second harmonic generation. The CARS contrast of these structural fibers may be useful if molecular spectroscopic information from the fibers is desired. In addition, tissue fat generates a very clear contrast, because of the high density of CH_2 modes. CARS microscopy is the method of choice for studies that require visualization of fat in tissues, which has been put to a good use in biomedical imaging studies concerned with obesity-related fat accumulation in mammary tissues[98] and atherosclerotic lipid deposits in arterial tissue.[65] More examples of lipid images will be given in the next section.

When addressed at the OH-stretching frequency, water also produces strong signals in the CARS imaging microscope. Visualizing tissue water at rapid image acquisition times is useful for following water diffusion and real-time hydration dynamics. The ability to monitor water diffusion is not only relevant to tissue biology, but has also found applications in food science. In Figure 11, for instance, the hydration process of water in cheese is mapped as a function of time, which reveals important information on how hydration depends on fat content.
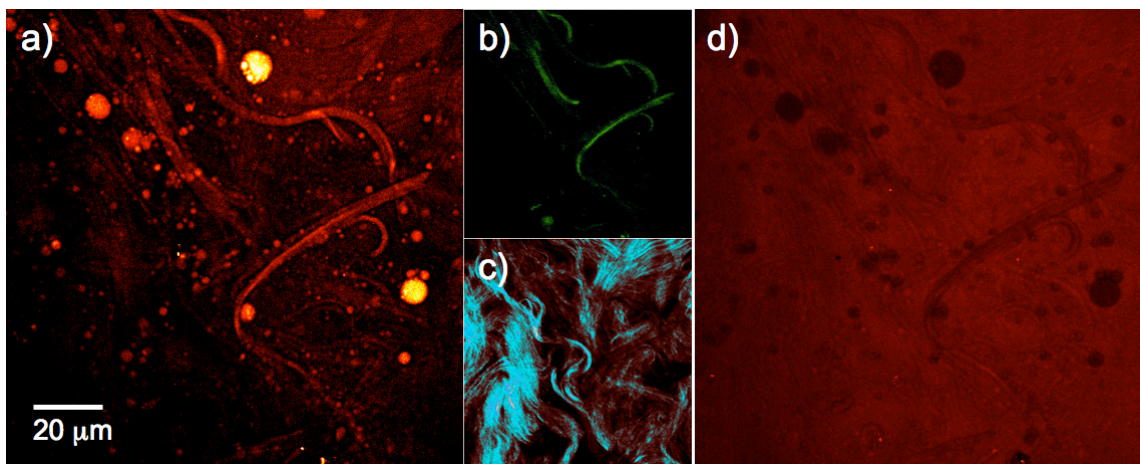

Figure 10: Typical tissue components seen with CARS microscopy. a) CARS image of human dermis at 2868 cm^{-1}, showing strong signals from lipid and elastin and a faint resonant signal from dermal collagen. b) TPEF image of elastin. c) SHG image of collagen. d) CARS image taken at 2993 cm^{-1}, off-resonance with the CH-stretching vibrations of lipid and structural protein, showing a clear contrast change with image a).
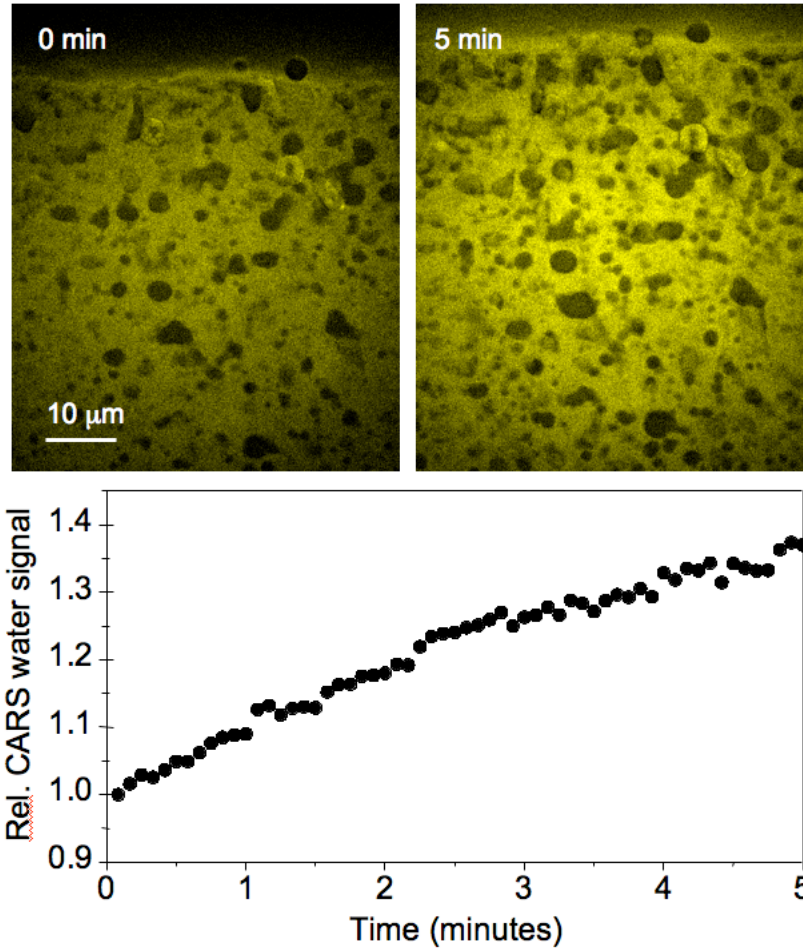
Figure 11: Hydration dynamics in cheese. Snapshots of cheese taken at OH-stretching vibration of water (3150 cm^{-1}) during a hydration experiment. Dark holes correspond to lipid clusters, which are off-resonance at this Raman shift. Brighter signals indicate higher water concentration over time. A slight swelling of the cheese is also seen. Bottom graph shows the relative increase of the CARS water signal over a time frame of 5 minutes. Courtesy of Friesland Foods Corporate Research, the Netherlands.

7. CARS biomedical imaging

7.1. Ex vivo nonlinear imaging

CARS is an excellent tool for examining tissues *ex vivo* without the need for labeling tissue components. The label-free approach enables investigation of tissue structures that are intact and not compromised by labeling protocols. Examining intact tissue is particularly important for disease-related research, where the biochemical and morphological characteristics of the diseased tissue need to be preserved for a proper analysis. Standard staining protocols are known to severely alter the morphology and integrity of the tissue, as well as to affect the presence of tissue fat. CARS is particularly

suitable to image lipids in intact tissues, as illustrated by the biomedical imaging examples below.

7.1.1. Lipid quantification in breast cancer tissue

Recent nuclear magnetic resonance (NMR) studies have shown that the concentration of NMR-visible lipids in breast cancer tissue is significantly lower compared to healthy tissue.[99, 100] The origin of this signature of cancer is unknown, although it has been suggested that a depletion of intracellular lipid droplets in cancer cells may play a major role. Lipid droplets, (sub)-micrometer sized bodies of neutral lipids, are a natural component of mammary epithelia.[14] In cancer cells, arrest of cell differentiation suppresses the formation of lipid droplets and decreases the corresponding lipid pool.[101-103] CARS is ideally suited to quantify the intracellular lipid droplet correlation and to correlate that with cell malignancy. Figure 12 shows that the number of lipid droplets in breast cancer cells in cell culture as visualized with CARS decreases with increasing malignancy of the cell. The challenge is to observe a similar trend in intact tissues. Figure 13 shows CARS imaging results from rat mammary tissue, a model system for human breast tissue. In combination with SHG imaging, the tumor region can be clearly identified. The inset shows furthermore that intracellular lipids can be visualized clearly in the three-dimensional tissue. Such imaging studies are further complemented by confocal Raman spectroscopic measurements for detailed chemical analysis of the lipid droplet content.
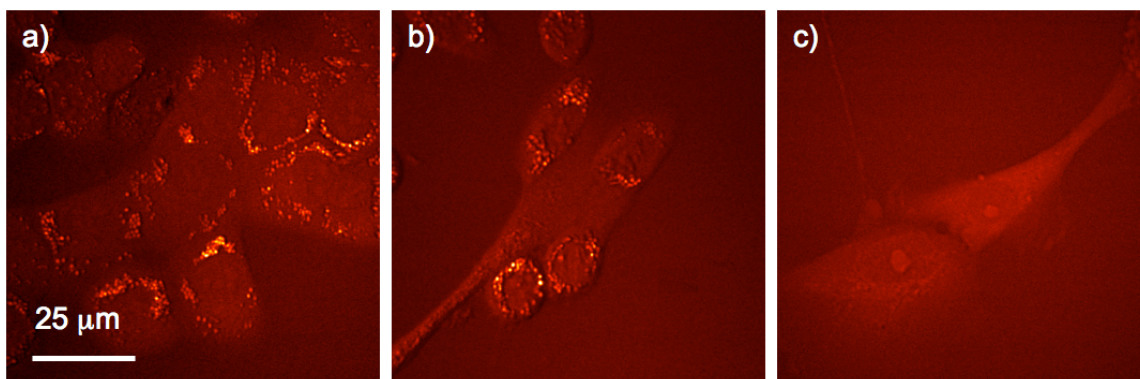

Figure 12: CARS images of a) live nonmalignant (MCF-12A); b) mildly malignant (MCF-7) and c), malignant (MBA-MB-231) breast cancer cells. The bright spots are the lipid droplets. Note that the droplet concentration in malignant cells is lower than in normal cells.
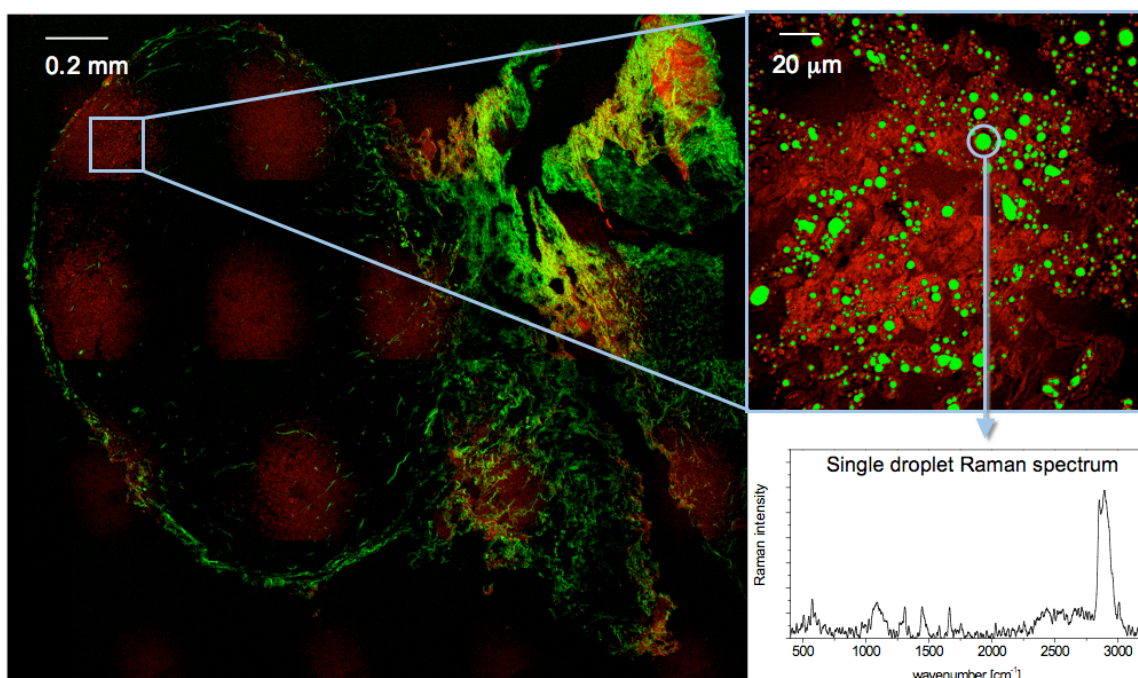
Figure 13: Label-free image of lipids in mammary tumor tissue. Left: large area (1.2 x 1.2 mm) image of lipid (CARS, red) and collagen (SHG, green). Right, top: high resolution image of tumor cells. The CH_2-contrast from cells is indicated in red and the CH_2-contrast from lipids has been color-coded green. Right, bottom: Raman spectrum of single lipid droplet. The CH_2 stretching vibrations in the 2850-3000 cm^{-1} range are easily identified.

7.1.2. Lipids in atherosclerotic lesions

Atherosclerosis is a disease that affects the walls of arterial blood vessels, forming pools of lipid-rich macrophages, smooth muscle cells, lipids, and components of the extracellular matrix. These lesions develop a fibrous encapsulation, which can become increasingly thin and may rupture as the lesion matures. Rupture of the fibrous cap causes the release of the inflammatory elements into the lumen, which, in turn, may obstruct blood flow.[104, 105] Multimodal CARS microscopy is ideally suited to characterize the different stages of the lesion. A CARS based methodology may eventually grow into a fiber-based diagnostic tool for early diagnosis of this arterial disease. Several studies on carotid arteries of Yorkshire pigs have underlined the potential of CARS microscopy for atherosclerosis research.[65, 84] Here we present the results of an imaging study on a mouse model system. The advantage of the ApoE-deficient mouse model is that it enables the study of atherosclerotic plaques as a function of multiple controllable parameters.

In Figure 14 a millimeter-sized piece of the aortic arch is shown for a mouse with disabled kidney function on a normal (Chow) diet. Several lesions of different degree of severity are recognized by the elevated levels of lipids. The lesions display different concentrations of macrophages, which are clearly identified in the zoomed-in CARS images. In combination with two-photon excited fluorescence contrast of elastin and SHG contrast of collagen, a comprehensive mapping of the major arterial tissue components was accomplished. Such 3D chemical maps of intact arterial tissue are

invaluable for a better understanding of atherosclerotic lesion development as a function of kidney function and diet.
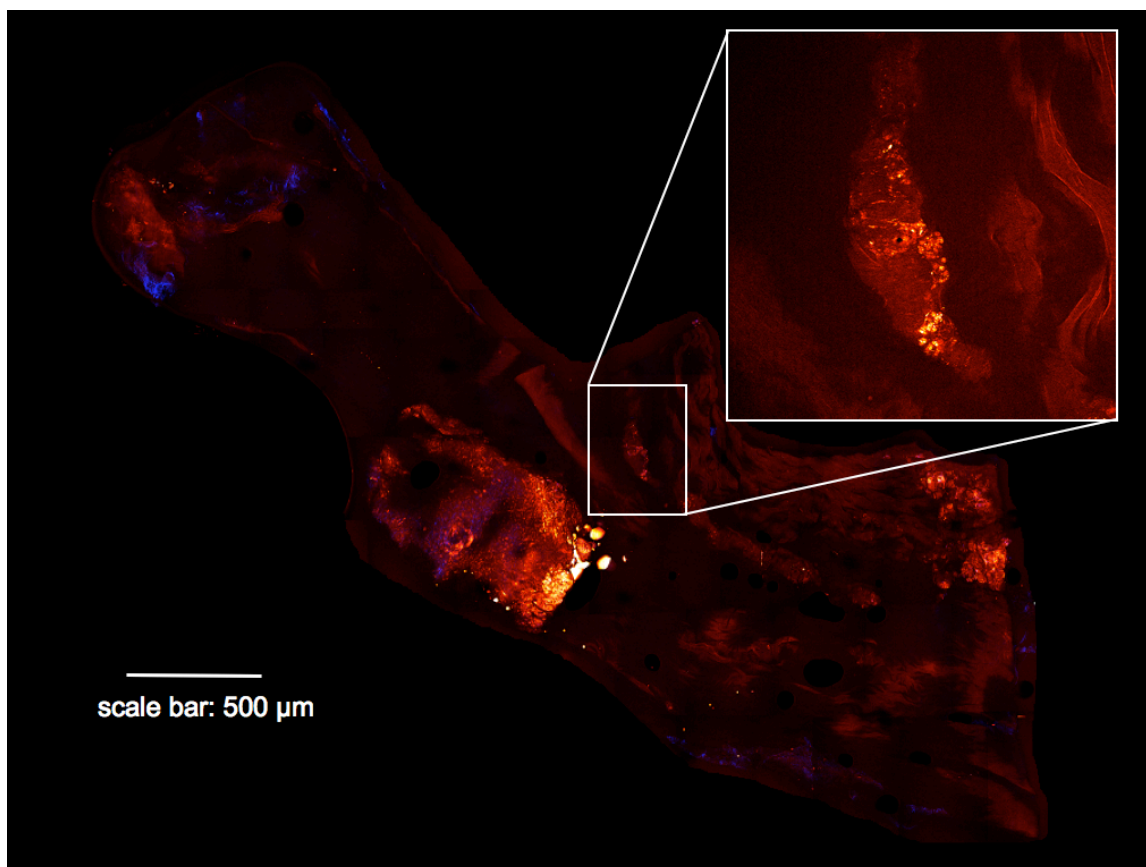

Figure 14: Large area composite CARS/SHG image of aorta of an ApoE deficient mouse. En face images were obtained from the luminal side at the lipid 2845 cm^{-1} signature band. CARS contrast is indicated in red/orange and SHG contrast in blue. Inset shows small atherosclerotic lesion at an early stage. Strong CARS signal from elastin of the blood vessel wall are also observed.

7.2. In vivo nonlinear imaging

For *in vivo* imaging applications, the issue of photodamage is particularly relevant. To limit tissue illumination in a particular location, fast scanning is imperative. When imaging fat in superficial tissue layers, the CARS signals are generally high enough to allow for video-rate imaging. At these rapid image acquisition times, localized tissue heating is minimized and photodamage can be reduced. Figure 15 shows the feasibility of *in vivo* imaging in a study concerned with visualizing lipid components in the mouse skin.[95] Important tissue structures such as lipid lamellae of the stratum corneum, sebaceous glands, dermal adipocytes and the fat containing cells of the subcutaneous layer are readily visualized with video-rate CARS. With imaging depths of up to several hundred micrometers, CARS microscopy constitutes a powerful method for investigating endogenous tissue structures in superficial layers without any form of labeling. *In vivo* biomedical imaging applications are just starting to emerge, but it is clear that CARS

microscopy has the potential to significantly contribute to basic scientific research and diagnostics of superficial tissues.
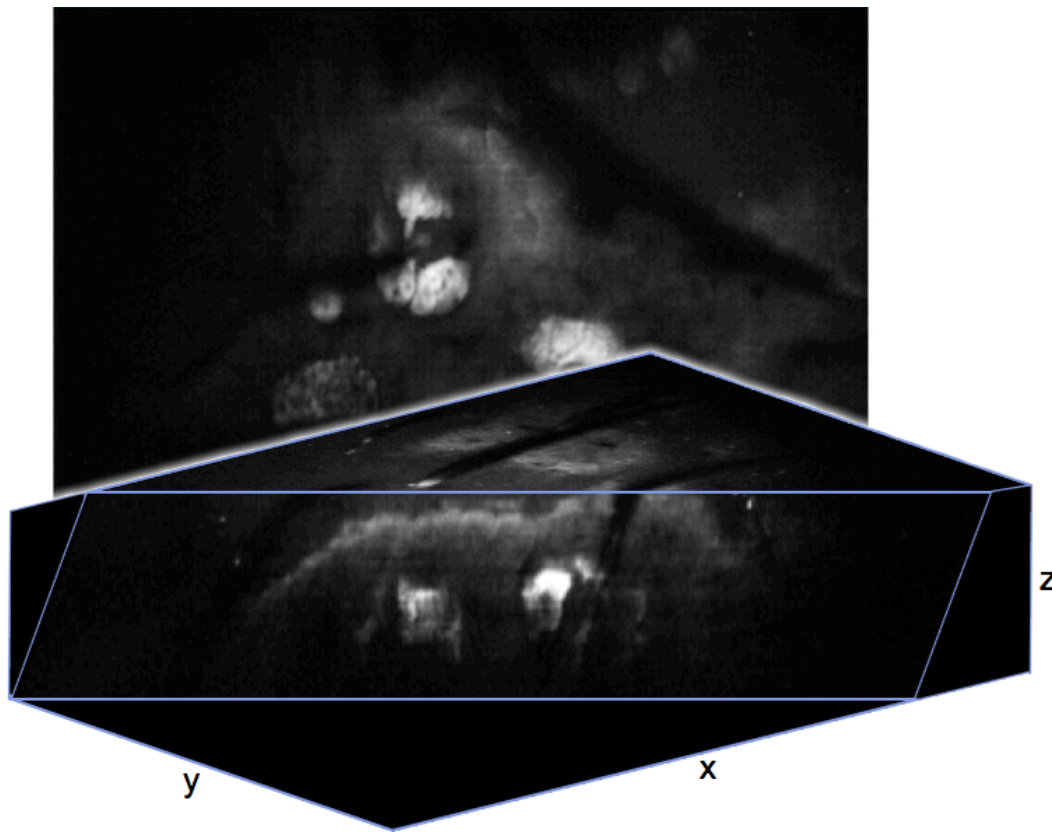

Figure 15: Three-dimensional CARS image with lipid contrast from mouse skin *in vivo*. Lipid-rich sebaceous glands near the hair follicle are clearly recognized. Data stack measures 800 x 640 x 125 μm^3.

8. What lies at the horizon

Since the inception of the second generation of CARS microscopes, the development of CARS microscopy has been characterized by steady technological advances. With robust laser technology and commercial CARS microscopes that are beginning to find the market, a new era of CARS microscopy has arrived in which the applications will be the driving force. The CARS technique has already proven to be a foremost imaging tool for lipids in cells and tissue. The lipid imaging capability will find many relevant applications in tissue biology, some of which are discussed in this Chapter. Biomedical applications also push the technology towards the integration of optical fibers and fiber-based probes. There is no doubt that such imaging extensions will become available for CARS microscopy in the near future, solidifying the technique's membership to the family of reliable biomedical imaging tools.

Acknowledgments

References

1. K. S. Krishnan and C. V. Raman, "A new type of secondary radiation," Nature **121**, 501-502 (1928).
2. G. Eckhardt, R. W. Hellwarth, F. J. McClung, S. E. Schwarz, and D. Weiner, "Stimulated Raman scattering from organic liquids," Phys. Rev. Lett. **9**, 455-457 (1962).
3. R. W. Hellwarth, "Analysis of stimulated Raman scattering of a giant laser pulse," Appl. Opt. **2**, 847-853 (1963).
4. R. W. Minck, R. W. Terhune, and W. G. Gado, "Laser-stimulated Raman effect and resonant four-photon interactions in gases H_2, D_2 and CH_4," Appl. Phys. Lett. **3**, 181-184 (1963).
5. P. D. Maker and R. W. Terhune, "Study of optical effects due to an induced polarization third order in the electric field strength," Phys. Rev. **137**, A801-818 (1965).
6. J. A. Armstrong, N. Bloembergen, J. Ducuing, and P. S. Pershan, "Interactions between light waves in a nonlinear dielectric," Phys. Rev. **127**, 1918-1939 (1962).
7. D. A. Kleinman, "Nonlinear dielectric polarization in optical media," Phys. Rev. **126**, 1977-1979 (1962).
8. M. D. Levenson, "Inteference of resonant and nonresonant three-wave mixing in diamond," Phys. Rev. B **6**, 3962-3965 (1972).
9. M. D. Levenson, "Feasibility of measuring the nonlinear index of refraction by third-order frequency mixing," IEEE J. Quant. Electron. **QE-10**, 110-115 (1974).
10. J. J. Wynne, "Nonlinear optical spectroscopy of $\chi^{(3)}$ in $LiNBO_3$," Phys. Rev. Lett. **29**, 650-653 (1972).
11. R. F. Begley, A. B. Harvey, and R. L. Byer, "Coherent anti-Stokes Raman spectroscopy," Appl. Phys. Lett. **25**, 387-390 (1974).
12. I. E. Harris and M. E. McIlwain, "Coherent anti-Stokes Raman spectroscopy in propellant flames," in *Fast Reactions in Energy Systems*, C. Capellos and R. F. Walker, eds. (Reidel, Boston, 1981).
13. R. J. Hall and A. C. Eckbreth, "Coherent anti-Stokes Raman spectroscopy: Applications to combustion diagnostics," in *Laser Applications*, R. K. Erf, ed. (Academic, New York, 1982).
14. A. C. Eckbreth, "CARS thermometry in practical combustors," Combust. Flame **39**, 133-147 (1980).
15. A. C. Eckbreth, P. A. Bonczyk, and J. F. Verdieck, "Combustion diagnostics by laser and fluorescence techniques," Prog. Energy Combust. Tech. **5**, 253-322 (1979).
16. A. Laubereau and W. Kaiser, "Vibrational dynamics of liquids and solids investigated by picosecond light pulses," Rev. Mod. Phys. **50**, 607-665 (1978).

17. R. Leonhardt, W. Holzapfel, W. Zinth, and W. Kaiser, "Terahertz quantem beats in molecular liquids," Chem. Phys. Lett. **133**, 373-377 (1987).
18. S. Mukamel, "Femtosecond optical spectroscopy: A direct look at elementary chemical events," Annu. Rev. Phys. Chem. **41**, 647-681 (1990).
19. K. A. Nelson and E. P. Ippen, "Femtosecond coherent spectroscopy," Adv. Chem. Phys. **75**, 1-35 (1989).
20. Y. Tanimura and S. Mukamel, "Femtosecond spectroscopy of liquids," J. Chem. Phys. **99**, 9496-9511 (1993).
21. M. Schmitt, G. Knopp, A. Materny, and W. Kiefer, "Femtosecond time-resolved coherent anti-Stokes Raman scattering for the simultaneous study of ultrafast ground and excited state dynamics: iodide vapour," Chem. Phys. Lett. **270**, 9-15 (1997).
22. M. Delhaye and P. Dhamelincourt, "Raman microprobe and microscope with laser excitation," J. Raman Spectrosc. **3**, 33-43 (1975).
23. M. Duncan, J. Reintjes, and T. J. Manuccia, "Scanning coherent anti-Stokes Raman microscope," Opt. Lett. **7**, 350-352 (1982).
24. A. C. Eckbreth, "BOXCARS: Crossed-beam phase-matched CARS generation in gases," Appl. Phys. Lett. **32**, 421-423 (1978).
25. M. D. Duncan, "Molecular discrimination and contrast enhancement using a scanning CARS microscope," Opt. Commun. **50**, 307-312 (1984).
26. M. D. Duncan, J. Reintjes, and T. J. Manuccia, "Imaging biological compounds using the CARS microscope," Opt. Engineering **24**, 352-355 (1985).
27. T. Scholten, "Coherent anti-Stokes Raman scattering (CARS): Technique and applications to biophysical studies; The potentials of CARS microscopy," (University of Twente, the Netherlands, Enschede, 1989).
28. I. Chabay, G. K. Klauminzer, and B. S. Hudson, "Coherent anti-Stokes Raman spectroscopy (CARS): Improved experimental design and observation of new higher-order processes " Appl. Phys. Lett. **28**, 27-29 (1976).
29. T. A. H. M. Scholten, G. W. Lucassen, F. F. M. d. Mul, and J. Greve, "Nonresonant background suppression in CARS spectra of dispersive media using phase mismatching," Appl. Opt. **28**, 1387-1400 (1989).
30. A. Zumbusch, G. Holtom, and X. S. Xie, "Vibrational Microscopy Using Coherent Anti-Stokes Raman Scattering," Phys. Rev. Lett. **82**, 4142-4145 (1999).
31. M. Müller, J. Squier, C. A. D. Lange, and G. J. Brakenhoff, "CARS microscopy with folded BoxCARS phasematching," J. Microsc. **197**, 150-158 (2000).
32. W. Denk, J. H. Strickler, and W. W. Webb, "Two-photon laser scanning fluorescence microscopy," Science **248**(4951), 73-76 (1990).
33. J. X. Cheng, A. Volkmer, L. D. Book, and X. S. Xie, "An epi-detected coherent anti-Stokes Raman scattering (E-CARS) microscope with high resolution and high sensitivity," J. Phys. Chem. B **105**, 1277-1280 (2001).
34. E. O. Potma, W. P. d. Boeij, P. J. M. v. Haastert, and D. A. Wiersma, "Real-time vizualization of intracellular hydrodynamics," Proc. Natl. Acad. Sci. USA **98**, 1577-1582 (2001).
35. J. X. Cheng, Y. K. Jia, G. Zheng, and X. S. Xie, "Laser-scanning coherent anti-Stokes Raman scattering microscopy and applications to cell biology," Biophys. J. **83**, 502-509 (2002).

36. X. Nan, J. X. Cheng, and X. S. Xie, "Vibrational imaging of lipid droplets in live fibroblast cells with coherent anti-Stokes Raman scattering microscopy," J. Lipid Res. **44**, 2202-2208 (2003).

37. J. X. Cheng, A. Volkmer, L. D. Book, and X. S. Xie, "Multiplex coherent anti-Stokes Raman scattering microspectroscopy and study of lipid vesicles," J. Phys. Chem. B **106**, 8493-8498 (2002).

38. M. Muller and J. M. Schins, "Imaging the thermodynamic state of lipid membranes with multiplex CARS microscopy," J. Phys. Chem B **106**, 3715-3723 (2002).

39. G. W. Wurpel, J. M. Schins, and M. Muller, "Direct measurement of chain order in single phospholipid mono- and bilayers with multiplex-CARS," J. Phys. Chem. B **108**, 3400-3403 (2004).

40. E. O. Potma and X. S. Xie, "Detection of single lipid bilayers with coherent anti-Stokes Raman scattering (CARS) microscopy," J. Raman Spectrosc. **34**, 642-650 (2003).

41. S. H. Lim, A. G. Caster, O. Nicolet, and S. R. Leone, "Chemical imaging by single pulse interferometric coherent anti-Stokes Raman scattering microscopy," J. Phys. Chem. B **110**, 5196-5204 (2006).

42. E. O. Potma, X. S. Xie, L. Muntean, J. Preusser, D. Jones, J. Ye, S. R. Leone, W. D. Hinsberg, and W. Schade, "Chemical imaging of photoresists with coherent anti-Stokes Raman scattering (CARS) microscopy," J. Chem. Phys. B **108**, 1296-1301 (2004).

43. B. G. Saar, H. S. Park, X. S. Xie, and O. D. Lavrentovich, "Three-dimensional imaging of chemical bond orientation in liquid crystals by coherent anti-Stokes Raman scattering microscopy," Opt. Express **15**, 13585-13596 (2007).

44. J. X. Cheng, "Coherent anti-Stokes Raman scattering microscopy," Appl. Spectrosc. **91**, 197-208 (2007).

45. J. X. Cheng and X. S. Xie, "Coherent anti-Stokes Raman scattering microscopy: instrumentation, theory and applications," J. Phys. Chem. B **108**, 827-840 (2004).

46. C. L. Evans and X. S. Xie, "Coherent anti-Stokes Raman scattering microscopy: chemical imaging for biology and medicine," Annu. Rev. Anal. Chem. **1**, 883-909 (2008).

47. A. Volkmer, "Vibrational imaging and microspectroscopies based in coherent anti-Stokes Raman scattering microscopy," J. Phys. D **38**, R59-R81 (2005).

48. S. Maeda, T. Kamisuki, and Y. Adachi, "Condensed phase CARS," in *Advances in Nonlinear Spectroscopy*, R. J. H. Clark and R. E. Hester, eds. (John Wiley and Sons Ltd., New York, 1988), pp. 253-297.

49. R. W. Boyd, *Nonlinear Optics* (Academic Press, San Diego, 2003).

50. E. O. Potma and X. S. Xie, "Theory of spontaneous and coherent Raman scattering," in *Handbook of Biological Nonlinear Optical Microscopy*, B. R. Masters and P. T. C. So, eds. (Oxford University Press, New York, 2008), pp. 164-185.

51. J. X. Cheng, L. D. Book, and X. S. Xie, "Polarization coherent anti-Stokes Raman scattering microscopy," Opt. Lett. **26**, 1341-1343 (2001).

52. F. Lu, W. Zheng, and Z. Huang, "Heterodyne polarization coherent anti-Stokes Raman scattering microscopy," Appl. Phys. Lett. **92**, 123901 (2008).

53. E. O. Potma, C. L. Evans, and X. S. Xie, "Heterodyne coherent anti-Stokes Raman scattering (CARS) imaging," Opt. Lett. **31**, 241-243 (2006).

54. F. Ganikhanov, C. L. Evans, B. G. Saar, and X. S. Xie, "High-sensitivity vibrational imaging with frequency modulation coherent anti-Stokes Raman scattering (FM-CARS) microscopy," Opt. Lett. **31**, 1872-1874 (2006).

55. F. Kajzar and J. Messier, "Third-harmonic generation in liquids," Phys. Rev. A **32**, 2352-2363 (1985).

56. X. Nan, E. O. Potma, and X. S. Xie, "Nonperturbative chemical imaging of organelle transport in living cells with coherent anti-Stokes Raman scattering microscopy," Biophys. J. **91**, 728-735 (2006).

57. L. Li, H. Wang, and J. X. Cheng, "Quantitative coherent anti-Stokes Raman scattering imaging of lipid distribution in coexisting domains," Biophys. J. **89**, 3480-3490 (2005).

58. A. Hopt and E. Neher, "Highly nonlinear photodamage in two-photon fluorescence microscopy," Biophys. J. **80**, 2029-2036 (2001).

59. A. Schönle and S. W. Hell, "Heating by absorption in the focus of an objective lens," Opt. Lett. **23**, 325-327 (1998).

60. K. Konig, P. T. C. So, W. W. Mantulin, and E. Gratton, "Cellular response to near-infrared femtosecond laser pulses in two-photon fluorescence microscopy," Opt. Lett. **22**, 135-136 (1997).

61. Y. Fu, H. Wang, and J. X. Cheng, "Characterization of photodamage in coherent anti-Stokes Raman scattering microscopy," Opt. Express **14**, 3942-3951 (2006).

62. T. Helllerer, C. Axäng, C. Brackmann, P. Hillertz, M. Pilon, and A. Enejder, "Monitoring of lipid storage in Caenorhabditis elegans using coherent anti-Stokes Raman scattering (CARS) microscopy," Proc. Natl. Acad. Sci. USA **104**, 14658-14663 (2007).

63. T. B. Huff and J. X. Cheng, "In vivo coherent anti-Stokes Raman scattering imaging of sciatic nerve tissues," J. Microsc. **225**, 175-182 (2007).

64. T. B. Huff, Y. Shi, Y. Yan, H. Wang, and J. X. Cheng, "Multimodel nonlinear optical microscopy and applications to central nervous system," IEEE J. Select. Topics. Quant. Electron. **14**, 4-9 (2008).

65. T. T. Le, I. M. Langohr, M. J. Locker, M. Sturek, and J. X. Cheng, "Label-free molecular imaging of atherosclerotic lesions using multimodal nonlinear optical microscopy," J. Biomed. Opt. **12**, 054007 (2007).

66. G. R. Holtom, B. D. Thrall, B. Y. Chin, H. S. Wiley, and S. D. Colson, "Achieving molecular selectivity in imaging using multiphoton Raman spectroscopy techniques " Traffic **2**, 781-788 (2001).

67. E. O. Potma and X. S. Xie, "Direct visualization of lipid phase segregation in single lipid bilayers with coherent anti-Stokes Raman scattering (CARS) microscopy," ChemPhysChem **6**, 77-79 (2005).

68. M. Diem, M. Romero, S. Boydston-White, M. Miljković, and C. Matthäus, "A decade of vibrational micro-spectroscopy of human cells and tissue (1994-2004)," Analyst. **129**, 880-885 (2004).

69. E. M. Vartiainen, H. A. Rinia, M. Muller, and M. Bonn, "Direct extraction of Raman line-shapes from congested CARS spectra," Opt. Express **14**, 3622-3630 (2006).

70. H. A. Rinia, M. Bonn, M. Müller, and E. M. Vartiainen, "Quantitative CARS spectroscopy using the maximum entropy method: The main lipid phase transition," ChemPhysChem **8**, 279-287 (2007).

71. M. Jurna, J. P. Korterik, C. Otto, and H. L. Offerhaus, "Shot noise limited heterodyne detection of CARS signals," Opt. Express **15**, 15207-15213 (2007).

72. G. I. Petrov, R. Arora, V. V. Yakovlev, X. Wang, A. V. Sokolov, and M. O. Scully, "Comparison of coherent and spontaneous Raman microspectroscopies for invasive detection of single bacterial endospores," Proc. Natl. Acad. Sci. USA **104**, 7776-7779 (2007).

73. C. A. Marx, U. Harbola, and S. Mukamel, "Nonlinear optical spectroscopy of single, few and many molecules: Nonequilibrium Green's function QED approach," Phys. Rev. A **77**, 022110 (2008).

74. M. Moskovits, "Surface-enhanced spectroscopy," Rev. Mod. Phys. **57**, 783-826 (1985).

75. A. Otto, I. Mrozek, H. Grabborn, and A. Akermann, "Surface-enhanced Raman scattering," J. Phys. Condens. Matter **4**, 1143-1212 (1992).

76. D. S. Chemla, J. P. Heritage, P. F. Liao, and E. D. Isaacs, "Enhanced four-wave mixing from silver particles," Phys. Rev. B **27**, 4553-4558 (1983).

77. M. Danckwerts and L. Novotny, "Optical frequency mixing at coupled gold nanoparticles," Phys. Rev. Lett. **98**, 026104, 026101-026104 (2007).

78. H. Kim, D. K. Taggart, C. Xiang, R. M. Penner, and E. O. Potma, "Spatial control of coherent anti-Stokes emission with height-modulated gold zig-zag nanowires," Nano Lett., in press (2008).

79. C. K. Shen, A. R. B. d. Castro, and Y. R. Shen, "Surface coherent anti-Stokes Raman spectroscopy," Phys. Rev. Lett. **43**, 946-949 (1979).

80. T. Ichimura, N. Hayazawa, M. Hashimoto, Y. Inouye, and S. Kawata, "Local enhancement of coherent anti-Stokes Raman scattering by isolated gold nanoparticles," J. Raman Spectrosc. **34**, 651-654 (2003).

81. T. Ichimura, N. Hayazawa, M. Hashimoto, Y. Inouye, and S. Kawata, "Tip-enhanced coherent anti-Stokes Raman scattering for vibrational nanoimaging," Phys. Rev. Lett. **92**, 220801 (2004).

82. T. W. Koo, S. Chan, and A. A. Berlin, "Single-molecule detection of biomolecules by surface-enhanced coherent Raman scattering," Opt. Lett. **30**, 1024 (2005).

83. E. O. Potma, D. J. Jones, J.-X. Cheng, X. S. Xie, and J. Ye, "High-sensitivity coherent anti-Stokes Raman scattering microscopy with two tightly synchronized picosecond lasers," Opt. Lett. **27**(13), 1168-1170 (2002).

84. H. W. Wang, T. T. Le, and J. X. Cheng, "Label-free imaging of arterial cells and extracellular matrix using a multimodal CARS microscope," Opt. Commun. **281**, 1813-1822 (2008).

85. W. R. Zipfel, R. M. Williams, R. Christie, A. Y. Nikitin, B. T. Hyman, and W. W. Webb, "Live tissue intrinsic emission microscopy using multiphoton-excited native fluorescence and sceond harmonic generation," Proc. Natl. Acad. Sci. USA **100**, 7075-7080 (2003).

86. W. R. Zipfel, R. M. Williams, and W. W. Webb, "Nonlinear magic: multiphoton microscopy in the biosciences," Nat. Biotechnol. **21**, 1369-1377 (2003).

87.   X. Deng and M. Gu, "Penetration depth of single-, two-, and three-photon fluorescence microscopic imaging through human cortex structures: Monte Carlo study," Appl. Opt. **42**, 3321-3329 (2003).

88.   R. Drezek, A. Dunn, and R. Richards-Kortum, "Light scattering from cells: finite-difference time domain similations and goniometric measurements," Appl. Opt. **38**, 3651-3661 (1999).

89.   A. K. Dunn, V. P. Wallace, M. Coleno, M. W. Berns, and B. J. Tromberg, "Influence of optical properties on two-photon fluorescence imaging in turbid samples," Appl. Opt. **39**, 1194-1201 (2000).

90.   B. Richards and E. Wolf, "Electromagnetic diffraction in optical systems II: Structure of the image field in an aplanatic system," Proc. Roy. Soc. A **253**, 358-379 (1959).

91.   F. Helmchen and W. Denk, "Deep tissue two-photon microscopy," Nat. Meth. **2**, 932-940 (2005).

92.   M. Rajadhyaksha, R. R. Anderson, and R. H. Webb, "Video-rate confocal scanning laser microscope for imaging human tissues in vivo," Appl. Opt. **38**, 2105-2115 (1999).

93.   J.-X. Cheng, A. Volkmer, and X. S. Xie, "Theoretical and experimental characterization of coherent anti-Stokes Raman scattering microscopy," J. Opt. Soc. Am. B **19**, 1363-1375 (2002).

94.   E. O. Potma, W. P. d. Boeij, and D. A. Wiersma, "Nonlinear coherent four-wave mixing in optical microscopy," J. Opt. Soc. Am. B **17**, 1678-1684 (2000).

95.   C. L. Evans, E. O. Potma, M. Puoris'haag, D. Cote, C. Lin, and X. S. Xie, "Chemical imaging of tissue *in vivo* with video-rate coherent anti-Stokes Raman scattering (CARS) microscopy," Proc. Natl. Acad. Sci. USA **102**, 16807-16812 (2005).

96.   F. Légaré, C. Pfeffer, and B. R. Olsen, "The role of backscattering in SHG tissue imaging," Biophys. J. **93**, 1312-1320 (2007).

97.   O. Nadiarnykh, R. B. LaComb, and P. J. Campagnola, "Coherent and incoherent SHG in fibrillar cellulose matrices," Opt. Express **15**, 3348-3360 (2007).

98.   T. T. Le, C. W. Rehrer, T. B. Huff, M. B. Nichols, I. G. Camarillo, and J. X. Cheng, "Nonlinear optical imaging to evaluate the impact of obesity on mammary gland and tumor stroma," Mol. Imaging **6**, 205-211 (2007).

99.   I. Barba, M. E. Cabanas, and C. Arus, "The relationship between nuclear magnetic resonance-visible lipids, lipid droplets, and cell proliferation in cultured c6 cells," Cancer Res. **59**, 1861-1868 (1999).

100.   L. L. Moyec, R. Tatoud, M. Eugene, C. Gauville, I. Primot, D. Charlemagne, and F. Calvo, "Cell and membrane lipid analysis by proton magnetic resonance spectroscopy in five breast cancer cell lines," Br. J. Cancer **66**, 623-628 (1992).

101.   E. J. Delikatny, W. A. Cooper, S. Brammah, N. Sathasivam, and D. C. Rideout, "Nuclear magnetic resonance-visible lipids induced by cationic lipophilic chemotherapeutic agents are accompanied by increased lippid droplet formation and damaged mitochondria," Cancer Res. **62**(1394-1400)(2002).

102.   K. Glunde, V. Raman, N. Mori, and Z. M. Bhujwalla, "RNA interference-mediated choline kinase suppression in breast cancer cells induces differentiation and reduces proliferation," Cancer Res. **65**, 11034-11043 (2005).

103. P. N. Munster, M. Srethapakdi, M. M. Moasser, and N. Rosen, "Inhibition of heat shock protein 90 function by ansamycins causes the morphological and functional differentionation of breat cancer cells," Cancer Res. **61**, 2945-2952 (2001).

104. J. Narula and H. W. Straus, "Imaging of unstable atherosclerotic lesions," Eur. J. Nucl. Med. Mol. Imaging **32**, 1-5 (2005).

105. R. Virmani, F. D. Kolodgie, A. P. Burke, A. V. Finn, H. K. Gold, T. N. Tulenko, S. P. Wrenn, and J. Narula, "Atherosclerotic plaque progression and vulnerability to rupture: Angiogenesis as a soruce of intraplaque hemorrhage," Artherioscler. Thromb. Vasc. Biol. **25**, 2054-2061 (2005).